

Theory of Semi-Deterministic Quantum Dot Placement in Heteroepitaxy

Zihang Wang^{1,*} and Dirk Bouwmeester^{1,2}

¹*Department of Physics, University of California Santa Barbara, Santa Barbara, California 93106, USA*

²*Huygens-Kamerlingh Onnes Laboratory, Leiden University, P.O. Box 9504, 2300 RA Leiden, Netherlands*

Achieving deterministic placement of self-assembled quantum dots (QDs) during epitaxial growth is essential for the reliable and efficient fabrication of high-quality single-photon sources and solid-state cavity quantum electrodynamics (cQED) systems, yet it remains a significant challenge due to the inherent stochasticity of QD nucleation processes. In this work, we theoretically demonstrate that deterministic QD nucleation within a pristine growth region can be achieved by engineering the boundary geometry of that region. During epitaxial growth, adatoms initially move toward the boundary and promote the formation of primary QDs along the boundary, driven by curvature and diffusion anisotropy. The resulting primary QDs distribution will generate many-body interactions that dynamically reshape the chemical potential landscape for subsequently deposited adatoms, enabling the formation of secondary QDs within the pristine growth region. These findings provide a theoretical foundation for reliable patterning of high optical-quality QDs, with potential applications in next-generation quantum photonic devices.

I. INTRODUCTION

Self-assembled semiconductor quantum dots (QDs) play a central role in on-chip quantum optics devices. Integrating QDs with optical microcavities, such as photonic crystals [1–3], microdisks [4], and micropillars [5–8], results in cavity quantum electrodynamics (cQED) systems capable of generating single photons on demand in a single optical mode via the Purcell effect. This capability is essential for implementing quantum cryptographic schemes and quantum communication networks [9–11].

With additional single electron charge control, QDs can be used to entangle photons with electron spins [12–16], enabling coherent transfer of quantum states between spin and photonic degrees of freedom [17, 18]. Such coherent light matter interactions at the single quantum level are essential for establishing distributed entanglement across quantum networks [19]. Recent achievements include the deterministic on-chip generation of spin photon entanglement in QDs [20], optical polarization and cooling of nuclear spin ensembles via the optical driving of a charged QD, enabling access and control at the single spin level [21], and the high efficiency generation of spin photon entangled states, a critical capability for future quantum repeater architectures [22].

The scaling of this semiconductor technology platform is however hampered by the fact that self-assembled QDs nucleate at random locations on the surface during molecular beam epitaxy (MBE). As a result, microcavities must either be carefully fabricated around pre-characterized QD locations (e.g., Refs. [23, 24]) or post-selection must be used to identify devices in which a QD happens to be well aligned with the cavity mode.

To avoid this time and resource consuming approach,

several attempts have been made to implement pre-patterned templates, such as those generated by buried stressors [25, 26] and capping layers [27, 28], to control adatom migration so that QD nucleation occurs at pre-determined locations. However, the accuracy with which these locations can be predicted is still influenced by surface asymmetric diffusion, strain resulting from lattice mismatch or surface imperfections, and the precise growth parameters [29–32]. The interplay of these effects remains largely unexplored, especially in efforts to predict QD spatial distributions under realistic growth conditions [33, 34].

Coarse-grained models have captured qualitative features observed in experiments. For example, kinetic Monte Carlo (KMC) simulations have demonstrated how pre-patterned substrates can direct and control nucleation sites [35]; phase-field simulations have reproduced QD densities comparable to experimental results on flat surfaces and have shown that surface patterns can guide QD nucleation, leading to more ordered dot placement [36].

While these theoretical models successfully capture the qualitative modulation of QD density resulting from strain fields, the role of spatiotemporal correlations in QD distributions, such as conditioning on previously formed QDs, has not yet been theoretically addressed.

We propose an overdamped Langevin framework demonstrating that semi-deterministic QD placement is theoretically achievable through the combined effects of geometry-defined boundary profiles and the secondary fields generated by previously nucleated QDs along the boundary. These boundary-anchored QDs dynamically reshape the chemical potential landscape via repulsive interactions, significantly modulating adatom diffusion kinetics and altering adatom trajectories beyond the boundary region. This stochastic formalism provides a comprehensive model for semi-deterministic spatial organization of QDs, opening new avenues for construct-

ing spatially ordered cQED systems for scalable quantum networks.

II. ADATOM DENSITY AND QD NUCLEATION IN THE QUASI-STATIONARY LIMIT

In traditional heteroepitaxy, atoms are deposited onto a planar substrate with effectively boundaries at infinity, under homogeneous temperature and stress conditions. The spatial adatom density is typically approximated as translationally invariant. As a result, nucleation sites are uniformly distributed across the entire substrate. QD nucleation typically occurs via the Stran-ski–Krastanov (SK) growth mode [37, 38]. This mode is one of the three primary epitaxial growth modes observed in thin-film deposition and is particularly relevant in heteroepitaxy where two different materials are involved (e.g., InAs on GaAs) [39]. It describes a transition from two-dimensional (2D) layer-by-layer growth to three-dimensional (3D) island formation. When deposition begins, the adatoms initially form a thin, flat wetting layer on the substrate surface. This layer grows coherently, adopting the lattice constant of the underlying substrate despite a lattice mismatch. As the wetting layer thickens, strain energy accumulates due to lattice mismatch between the film and the substrate (e.g., InAs has a $\sim 7\%$ larger lattice constant than GaAs) [40]. After reaching a critical thickness, typically a few monolayers, the strain energy induces local instabilities that trigger the spontaneous formation of three-dimensional islands. Adatoms begin to aggregate at these energetically favorable sites and form nanometer-sized clusters, resulting in the formation of QDs. The density and size of these dots can be tuned based on the growth conditions.

Adatoms exhibit anisotropic diffusion, and arsenic (As) adatoms tend to form surface dimers upon attachment, resulting in dimer row or valley structures. Indium (In) atoms diffuse with significantly different rates depending on whether their motion is tangential, which is slower and aligned along $\hat{\mathbf{y}} \equiv [1\bar{1}0]$, or orthogonal, which is faster and aligned along $\hat{\mathbf{x}} = [110]$, to the As dimer rows [41]. This directional anisotropy can lead to elongated quantum dots aligned along the fast diffusion axis $[1\bar{1}0]$ [42].

As suggested by several recent experimental studies, the introduction of boundary fields may arise from local strain gradients, such as those generated by buried stressors [25, 26] and capping layers [27, 28], or from thermal gradients across the substrate. As illustrated in Fig.1, we present several examples of boundary fields that can be parametrized either by arc length or by the shape of composite geometries. We classify boundary fields into three types: exterior, interior, and soft boundary fields. Both exterior and interior fields correspond to hard physical boundaries (for example, hard mask edges) that adatoms

cannot physically penetrate during the epitaxy process. In contrast, a soft boundary field, such as one induced by buried stressors, is associated with partially forbidden regions where adatom migration is energetically unfavorable during growth, for example, in regions exhibiting thermal or strain gradients. Boundary field strengths, governed by in-plane compressive strain and local impurities, can alter the diffusion dynamics of adatoms during epitaxy, resulting in an increased likelihood of quantum dot nucleation within or near the defined boundary region. We refer to the exposed pristine surface (white-colored regions in Fig.1) as the bulk in this work.

The dynamics of the adatom density field are governed by the two-dimensional continuity equation, which relates the temporal change in density to the divergence of the adatom flux,

$$\partial_t n(\mathbf{r}, t) + \nabla \cdot \mathbf{J}(\mathbf{r}, n, B, t) = 0, \quad (1)$$

where $\mathbf{J}(\mathbf{r}, n, B, t)$ is the local adatom current density, \mathbf{r} is the spatial coordinate, t is time, and $B = \int du B[\mathbf{r} - \mathbf{r}_{\text{bd}}(u)]$ represents the spatially varying boundary field strength at \mathbf{r} . The boundary field is parameterized by u , the arc-length variable along the boundary, and $\mathbf{r}_{\text{bd}}(u)$ denotes the unit-speed spatial parametrization of the boundary at u . We note that, in general, the boundary field is a tensor that captures structural coupling within the boundary contour. In this work, without loss of generality of our method, we assume that $B[\mathbf{r} - \mathbf{r}_{\text{bd}}(u)]$ is a scalar field.

The adatom number conservation expressed above holds approximately under the assumption that the epitaxy rate is much slower than the timescale required for adatom diffusion to reach a quasi-steady state. To model the atom deposition process during epitaxy, we introduce adatoms uniformly across the exposed substrate area, with a deposition rate that is significantly smaller than the diffusion timescale. We refer to this regime as the quasi-stationary limit.

In the quasi-stationary limit, the evolution of the adatom density is governed by the coupled dynamics of the local adatom density $n(\mathbf{r})$ and the associated density flux $\mathbf{J}(\mathbf{r})$, described by the Boltzmann weight $P[n(\mathbf{r}), \mathbf{J}(\mathbf{r})]$,

$$P[n, \mathbf{J}] = \frac{1}{\mathcal{Z}} \exp \left[-\frac{1}{k_B T} H[n, \mathbf{J}, B] \right], \quad (2)$$

where $H[n(\mathbf{r}), \mathbf{J}(\mathbf{r}), B]$ is a general many-body correlation functional associated with the field configuration $[n, \mathbf{J}]$, and \mathcal{Z} is the partition function, defined as the functional integral $\mathcal{Z} = \int \mathcal{D}n \mathcal{D}\mathbf{J} P[n, \mathbf{J}]$ over all admissible field configurations.

The QD nucleation probability at a site \mathbf{r} depends on the ensemble average over all density and flux fields and takes the form,

$$P_{\text{QD}}(\mathbf{r}) = \frac{1}{\mathcal{Z}} \int \mathcal{D}n \mathcal{D}\mathbf{J} P[n, \mathbf{J}] \lambda(n(\mathbf{r}), \mathbf{J}(\mathbf{r})), \quad (3)$$

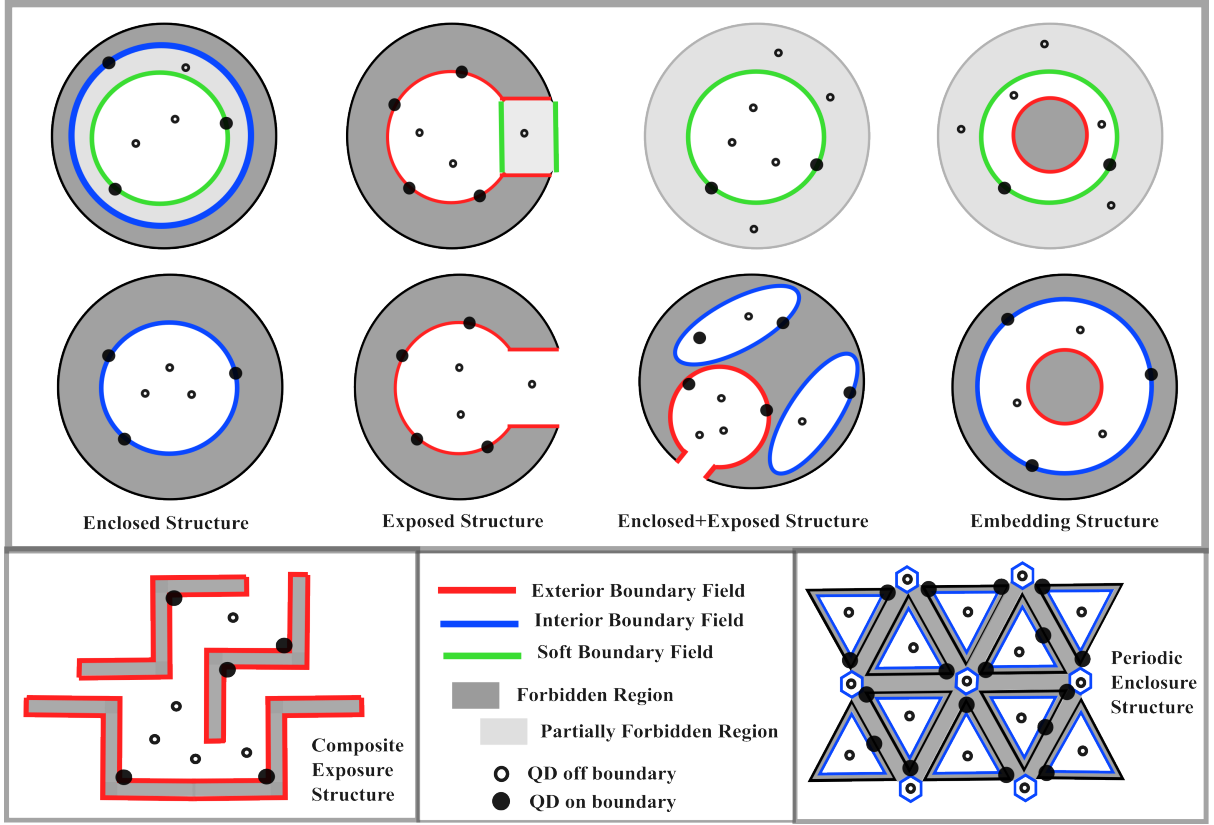


FIG. 1. Illustration of patterned geometries used to generate engineered boundary fields (e.g., strain fields). Red and blue lines indicate the boundary contours of patterned regions that induce localized field gradients. For illustrative purposes, solid black circles represent QD nucleating directly at these boundaries, while open circles denote QDs formed under the collective influence of both the boundary fields and QDs already formed on the boundary. Various pattern geometries demonstrate the flexibility of geometric design in controlling the spatial distribution of boundary-induced QD nucleation. The dark gray regions represent areas that adatoms cannot physically access, such as hard masks (forbidden regions), while light gray regions denote areas where adatom access is energetically unfavorable (partially forbidden). We refer to the exposed pristine surface (white regions) as the bulk in this work.

where $\lambda(n(\mathbf{r}), \mathbf{J}(\mathbf{r}))$ is the local nucleation rate function, modeled as,

$$\lambda(n, \mathbf{J}) = \lambda_0 \cdot \Theta(n - n_{\text{crit}}) \cdot \mathcal{R}(n, \mathbf{J}), \quad (4)$$

with n_{crit} denoting the critical adatom density for QD nucleation. Here, Θ is the Heaviside step function, and $\mathcal{R}(n, \mathbf{J})$ is a modulation factor that may be modeled as a delta function $\delta(n - n_{\text{crit}})$, or a smooth exponential dependence on n and \mathbf{J} .

While this expression for the nucleation probability is formally exact in the quasi-stationary limit, the high-dimensional structure of the functional renders analytical treatment infeasible in most practical scenarios.

Direct sampling of the distribution $P[n, \mathbf{J}]$ is computationally intractable due to nonlocal correlations and nonlinear coupling between the adatom density $n(\mathbf{r})$ and flux $\mathbf{J}(\mathbf{r})$ embedded in the functional $H[n, \mathbf{J}, B]$. Consequently, conventional importance-sampling methods are often inefficient or unstable. To overcome this challenge, we adopt a stochastic sampling approach based

on Langevin dynamics, which enables Monte Carlo sampling of field configurations according to the Boltzmann weight $\exp[-H[n, \mathbf{J}, B]/(k_B T)]$. In this framework, the time evolution of $n(\mathbf{r}, t)$ and $\mathbf{J}(\mathbf{r}, t)$ is governed by coupled Langevin equations that incorporate both deterministic drift toward the minimum of $H[n, \mathbf{J}, B]$ and stochastic noise consistent with thermal fluctuations, in accordance with the fluctuation-dissipation theorem [43]. The steady-state solution of the corresponding Fokker-Planck equation yields the quasi-stationary distribution $P[n, \mathbf{J}]$ [44]. This approach allows efficient exploration of the high-dimensional field space and accurate estimation of ensemble-averaged observables, including the spatially resolved QD nucleation probability $P_{\text{QD}}(\mathbf{r})$.

III. EMPIRICAL FIELD, QD NUCLEATION, AND LANGEVIN-BASED MONTE CARLO SAMPLING

To sample the quasi-stationary field configurations from $P[n, \mathbf{J}]$, we introduce a discrete empirical adatom density field $\hat{n}(\mathbf{r}, t)$ and empirical current density $\hat{\mathbf{J}}(\mathbf{r}, t)$, defined as sums over Dirac delta functions centered on an ensemble of adatoms $\{\mathbf{r}_i\}$, where each adatom is labeled by an index i ,

$$\hat{n}(\mathbf{r}, t) = \sum_{i=1}^N \delta(\mathbf{r} - \mathbf{r}_i(t)), \quad \hat{\mathbf{J}}(\mathbf{r}, t) = \sum_{i=1}^N \frac{d\mathbf{r}_i(t)}{dt} \delta(\mathbf{r} - \mathbf{r}_i(t)), \quad (5)$$

which satisfy the continuity equation by construction.

We assume that adatoms are initially deposited uniformly onto the surface Ω , so that $\hat{n}(\mathbf{r}, 0) \sim 1/\Omega$, with Ω being the surface area, and each adatom i undergoes stochastic evolution governed by the following overdamped Langevin dynamics ($k_B T \equiv 1$),

$$m \frac{d^2 \mathbf{r}_i}{dt^2} \approx 0 = -\mathbf{\Gamma} \frac{d\mathbf{r}_i}{dt} - \nabla_i U_{\text{sys}} + \sqrt{2\mathbf{\Gamma}} \boldsymbol{\eta}_i(t), \quad (6)$$

where m is the effective mass, $\mathbf{\Gamma}$ is the friction tensor (assumed diagonal) along the two principal crystallographic directions $[1\bar{1}0]$ and $[110]$, and $\boldsymbol{\eta}_i(t)$ is a Gaussian noise term (a *distribution*) with statistics $\langle \eta_i(t) \eta_j(t') \rangle = \delta_{ij} \delta(t - t')$.

The total microscopic potential energy U_{sys} includes both the boundary field B and pairwise interactions w , defined as a functional of the empirical adatom density field over the entire exposed substrate area Ω ,

$$U_{\text{sys}}[\hat{n}] = \int_{\Omega} du \int_{\Omega} B[\mathbf{r} - \mathbf{r}_{\text{bd}}(u)] \hat{n}(\mathbf{r}, t) d\mathbf{r} + \frac{1}{2} \iint_{\Omega} \hat{n}(\mathbf{r}, t) w(\mathbf{r} - \mathbf{r}') \hat{n}(\mathbf{r}', t) d\mathbf{r} d\mathbf{r}'. \quad (7)$$

By summing over all adatoms i , the empirical density field evolves according to the following stochastic differential equation (SDE),

$$\frac{\partial \hat{n}(\mathbf{r}, t)}{\partial t} = \nabla \cdot [\hat{n}(\mathbf{r}, t) \mathbf{D} \nabla \mu(\mathbf{r}, t)] + \nabla \cdot [\sqrt{2\hat{n}(\mathbf{r}, t) \mathbf{D}} \boldsymbol{\eta}(\mathbf{r}, t)], \quad (8)$$

where the diffusion tensor is given by $\mathbf{D} = \mathbf{\Gamma}^{-1}$, and the functional derivative $\mu = \delta U_{\text{sys}} / \delta \hat{n}(\mathbf{r}, t)$ represents the single-adatom chemical potential, and its spatial gradient $-\nabla \mu$ corresponds to the microscopic force acting on the adatom ensemble. In this framework, the total force is modeled as the sum of a boundary-induced term and pairwise interaction contributions,

$$\mu(\mathbf{r}, t) = \nabla \frac{\delta U_{\text{sys}}}{\delta \hat{n}(\mathbf{r}, t)} = \int_{\Omega} du B[\mathbf{r} - \mathbf{r}_{\text{bd}}(u)] + \int_{\Omega} w(\mathbf{r} - \mathbf{r}') \hat{n}(\mathbf{r}', t) d\mathbf{r}' \quad (9)$$

Although this expression is formally valid, the functional derivative is not rigorously defined due to the singular nature of \hat{n} , which consists of Dirac delta functions. In practice, force gradients are computed directly from the adatom-level Langevin dynamics. Thus, the SDE above should be interpreted as describing the stochastic evolution of an adatom ensemble, rather than as a coarse-grained partial differential equation (PDE).

To sample the density field $\hat{n}(\mathbf{r}, t)$, we do not solve the above SDE directly. Instead, we simulate Langevin dynamics for an ensemble of N adatoms and estimate the empirical field via a grid-based Monte Carlo technique. Specifically, we evolve the single-adatom Langevin equation given in Eq. 6,

$$\frac{d\mathbf{r}_i}{dt} = -\mathbf{D} \nabla_i U_{\text{sys}} + \sqrt{2\mathbf{D}} W_i(t), \quad (10)$$

where $W_i(t)$ is a standard Wiener process. From the resulting trajectories, the empirical adatom density field is computed by counting particles on a spatial grid element $d\Omega$, parametrized by the two-dimensional variable \mathbf{l} , centered at \mathbf{r}_0 and covering the exposed substrate region Ω . This yields a time-dependent realization of the empirical field that satisfies the above SDE in expectation over ensemble averages,

$$\hat{n}(\mathbf{r}) \approx \frac{1}{d\Omega} \sum_i \int_{d\Omega} d\mathbf{l} \delta(\mathbf{r}_i - \mathbf{r} + \mathbf{l}). \quad (11)$$

The above Langevin formulation, which generates the empirical adatom density field, must also incorporate microscopic nucleation processes that lead to QD formation during heteroepitaxy. To account for this, we define the local nucleation free energy $G(\hat{n}, \mathbf{r}_0)$ as the free energy cost to assemble a cluster of \hat{n} adatoms within a grid cell of width $\sqrt{d\Omega}$, centered at \mathbf{r}_0 . This nucleation barrier is computed by evaluating the system free energy $U_{\text{sys}}[\hat{n}(\mathbf{r}, t)]$ on a constrained configuration in which n adatoms are localized near \mathbf{r}_0 , and subtracting the reference free energy of the homogeneous background state $\hat{n}(\mathbf{r}, 0) \sim 1/\Omega$,

$$G(\hat{n}, \mathbf{r}_0) = U_{\text{sys}}[\hat{n}(\mathbf{r}_0, t)] - U_{\text{sys}}[\hat{n}(\mathbf{r}_0, 0)]. \quad (12)$$

The function $G(\hat{n}, \mathbf{r}_0)$ captures the energetic trade-off between inter-adatom interactions, entropic spreading, strain relaxation, and the influence of boundary fields near \mathbf{r}_0 . Typically, $G(\hat{n}, \mathbf{r}_0)$ exhibits two local minima and one maximum with respect to \hat{n} , corresponding to metastable and stable nucleation states separated by a free energy barrier [45].

To model the nucleation process under thermal fluctuations, we introduce a localized seed potential V_{seed} at \mathbf{r}_0 whenever the empirical density exceeds a subcritical threshold n_{seed} . This seed persists for a finite duration τ_c , during which the system is allowed to either evolve

toward the critical density n_{crit} , corresponding to the second minimum of G , or decay back to the metastable uniform state. If the empirical density reaches n_{crit} within the time window τ_c , the seed potential is irreversibly converted into a stable QD potential V_{QD} , indicating successful traversal of the nucleation barrier. Otherwise, the potential is removed, corresponding to dissolution due to thermal fluctuations.

In general, the seeding potential V_{seed} is attractive, promoting local adatom accumulation and cluster formation. Once a QD reaches a characteristic size determined by the growth conditions, further adatom attachment becomes energetically unfavorable. Therefore, the QD potential V_{QD} is modeled as repulsive, reflecting the stabilization of the dot and the inhibition of further growth beyond its stationary size.

The above construction captures the stochastic nature of nucleation. This concept is formalized through a time-dependent nucleation potential centered at \mathbf{r}_0 , evolving as,

$$V_{\text{nc}}(\mathbf{r}-\mathbf{r}_0, t) = \begin{cases} V_{\text{seed}}(\mathbf{r}-\mathbf{r}_0, t), & \text{if } |t-t_0| \leq \tau, \\ V_{\text{QD}}(\mathbf{r}-\mathbf{r}_0), & \text{if } \hat{n}(\mathbf{r}_0, t) \geq n_{\text{crit}}, \\ 0, & \text{otherwise (dissolution),} \end{cases} \quad (13)$$

where the seed lifetime τ is drawn from an exponential distribution, $\tau \sim \exp(1/\tau_c)$, and t_0 denotes the first-passage time for seeding, defined as,

$$t_0 = \min \{t \mid \hat{n}(\mathbf{r}_0, t) \geq n_{\text{seed}}\}. \quad (14)$$

If no QD nucleation occurs within the interval $[t_0, t_0 + \tau]$, the potential is reset and the seeding process restarts at position \mathbf{r} . The system energy is updated by incorporating the time-dependent nucleation potential,

$$U_{\text{sys}} \rightarrow U_{\text{sys}} + \frac{1}{2} \iint_{\Omega} \hat{n}(\mathbf{r}, t) V_{\text{nc}}(\mathbf{r}-\mathbf{r}_0, t) \hat{n}(\mathbf{r}_0, t) d\mathbf{r} d\mathbf{r}_0, \quad (15)$$

and the Langevin dynamics is modified accordingly.

Without loss of generality, we adopt the following interaction forms in the simulations presented in this work. The boundary field is modeled as a delta-function sink potential, modulated by the (dimensionless) local strain profile $\sigma[\mathbf{r}_{\text{bd}}(u)]$, which prevents adatoms from escaping once they reach the boundary,

$$B[\mathbf{r}-\mathbf{r}_{\text{bd}}(u)] = -B_0 \sigma[\mathbf{r}_{\text{bd}}(u)] \delta[\mathbf{r}-\mathbf{r}_{\text{bd}}(u)]. \quad (16)$$

This formulation allows adatoms to migrate tangentially along the boundary. The sign of the strain profile σ encodes the local stress state: compressive strain (positive σ) attracts adatoms, while tensile strain (negative σ) repels them. While in general, the boundary field strength would vary due to inhomogeneity along the boundary

profile, we assume that the strain results from local lattice mismatch and thus depends only on the local boundary curvature.

The pairwise repulsion between adatoms, w , and the nucleation potentials, V_{nc} , are modeled using a screened power-law (Yukawa-like) potential V , expressed as,

$$V(\mathbf{r}-\mathbf{r}') = \frac{\exp\left[-\left|\sqrt{2\mathbf{D}/\lambda}(\mathbf{r}-\mathbf{r}')\right|\right]}{\left|\sqrt{2\mathbf{D}/\lambda}(\mathbf{r}-\mathbf{r}')\right|^\alpha}, \quad (17)$$

where λ is the finite adatom lifetime, associated with a constant evaporation rate. The power-law exponent α is microscopic parameter that characterizes the strength and range of the many-body interactions.

IV. LINEAR PERTURBATION THEORY IN THE DILUTED LIMIT

In the early stage of the heteroepitaxy, thermally driven stochastic migration of adatoms leads to preferential deposition toward boundary edges that are orthogonal to the fast diffusion axis $\hat{\mathbf{x}} \equiv [1\bar{1}0]$, followed by lateral spreading along the boundary, as demonstrated numerically in Fig. 2C. When the average empirical density \hat{n} over the exposed region Ω remains much smaller than the homogeneous density limit $\hat{n}_{\text{hm}} = \Omega/\lambda_w^2$, the adatom dynamics are primarily governed by anisotropic diffusion. We refer to this regime as the *diluted limit*, where the exposed region Ω remains effectively adatom-free.

It is important to note that, locally, the empirical density may exceed this limit on the boundary. Depending on the repulsion strength between adatoms and the critical seeding density, such local accumulation can initiate the early stages of quantum dot nucleation.

We coarse-grain the empirical field \hat{n} into a continuous density field n , and introduce a decay term to account for the finite lifetime of adatoms, characterized by a constant evaporation rate λ . Expanding locally around a boundary point $\mathbf{r}_{0,\text{bd}} = (x_0, y_0)$, we assume that the convection–reaction–diffusion dynamics are separable to linear order along the principal axes. This yields a local density field n_0 , modulated by separable spatial factors $f(x-x_0)$ and $g(y-y_0)$, such that,

$$n(\mathbf{r}_{\text{bd}}) = f(x-x_0) \cdot g(y-y_0) \cdot n_0 \Rightarrow \ln n = \ln f + \ln g + \ln n_0. \quad (18)$$

Near the boundary point $\mathbf{r}_{0,\text{bd}}$, the change in current density along the boundary curve is given by

$$\frac{d\mathbf{J}}{ds}(\mathbf{r}_{\text{bd}}) = \frac{dJ_{\parallel}}{ds} \hat{\mathbf{T}} + J_{\parallel} \frac{d\hat{\mathbf{T}}}{ds} = \frac{dJ_{\parallel}}{ds} \hat{\mathbf{T}} + \kappa J_{\parallel} \hat{\mathbf{N}}, \quad (19)$$

where $\kappa(\mathbf{r}_{0,\text{bd}})$ is the local curvature, describing how rapidly the boundary turns at $\mathbf{r}_{0,\text{bd}}$. The vectors $\hat{\mathbf{T}}$ and $\hat{\mathbf{N}}$ are the local tangent and outward normal vectors, respectively, evaluated at the boundary.

The tangential component of the current density is defined as,

$$J_{\parallel}(\mathbf{r}_{\text{bd}} - \mathbf{r}_{0,\text{bd}}) = -\hat{\mathbf{T}} \cdot \mathbf{D} \nabla n, \quad \kappa(\mathbf{r}_{0,\text{bd}}) \cdot \hat{\mathbf{T}} \cdot \mathbf{D} \nabla n \geq 0, \quad (20)$$

and, for consistency, we adopt the convention that the adatom flow aligns with the direction in which the boundary turns. This convention does not affect the physical direction of adatom motion but serves to interpret the sign of the local current density magnitude. Positive values correspond to accumulation, while negative values indicate depletion, with the sign further modulated by the local strain profile.

The local continuity equation at the boundary point $\mathbf{r}_{0,\text{bd}}$ is given by,

$$\partial_t n = -\hat{\mathbf{T}} \cdot \nabla J_{\parallel} - \kappa \text{Sign}[\sigma(\mathbf{r}_{0,\text{bd}})] J_{\parallel} - \lambda n, \quad (21)$$

where the sign of the local strain profile, $\text{Sign}[\sigma(\mathbf{r}_{0,\text{bd}})]$, determines the nature of the curvature-driven contribution: compressive strain ($\text{Sign} = +1$) promotes adatom accumulation over time, while tensile strain ($\text{Sign} = -1$) drives depletion.

Substituting the expression for J_{\parallel} into the Eq. 21, we have,

$$\hat{\mathbf{T}} \cdot \nabla \left(\hat{\mathbf{T}} \cdot \mathbf{D} \nabla n \right) + \text{Sign}[\sigma(\mathbf{r}_{0,\text{bd}})] \kappa \left(\hat{\mathbf{T}} \cdot \mathbf{D} \nabla n \right) - \lambda n = 0, \quad (22)$$

which can be separated into a system of two PDEs for $f(x - x_0)$ and $g(y - y_0)$, respectively.

Expanded in Cartesian components around the boundary point $\mathbf{r}_{0,\text{bd}}$, the local convection–diffusion–reaction equations take the form

$$\begin{aligned} \frac{\partial f}{\partial t} &= T_x^2 D_x \frac{\partial^2 f}{\partial x^2} + \kappa T_x D_x \frac{\partial f}{\partial x} - \lambda f, \\ \frac{\partial g}{\partial t} &= T_y^2 D_y \frac{\partial^2 g}{\partial y^2} + \kappa T_y D_y \frac{\partial g}{\partial y} - \lambda g, \end{aligned} \quad (23)$$

where $T_x = \hat{\mathbf{T}} \cdot \hat{\mathbf{x}}$ and $T_y = \hat{\mathbf{T}} \cdot \hat{\mathbf{y}}$ denote the projections of the local tangent direction along the two principal diffusion axes. These equations are invariant under parity transformation ($x \rightarrow -x$, $y \rightarrow -y$).

The first-order expansion near a boundary point elucidates the interplay between anisotropic diffusion and geometric modulation, yielding a tractable expression for the stationary adatom density profile along and near the boundary. The general steady-state solution of the adatom density field can be constructed as a product of first-order expansions using the boundary parametrization u , where θ is the corresponding angular variable,

$$\frac{n(u_N)}{n_0} = \prod_{i=0}^N \sum_{c, c' = \pm 1} A_{c, c'}^i \exp \left[du_i \left(k_x^c |T_x(u_i)| + k_y^{c'} |T_y(u_i)| \right) \right] \quad (24)$$

where $A_{c, c'}^i$ is a coefficient determined by boundary conditions and local geometry, and du_i denotes the local

boundary segment at u_i . Recall that $\mathbf{r}_{\text{bd}}(u)$ is a unit-speed trajectory ($|\mathbf{dr}_{\text{bd}}(u)/du| = 1$), we have,

$$\frac{dv_i}{du_i} = |T_v(u_i)| \approx \frac{|v(\theta_{i+1}) - v(\theta_i)|}{du_i}, \quad v = x, y, \quad (25)$$

where $v = x, y$ labels the primary diffusion axes. The exponent in Eq. 24 can be compactly written as (Appendix A),

$$\begin{aligned} k_v^c |T_v(u_i)| &= \frac{\kappa(u_i)}{2} + c \mathcal{K}_v(u_i), \\ \ell_v &= \sqrt{\frac{D_v}{\lambda}}, \quad \mathcal{K}_v(u_i) = \sqrt{\left[\frac{\kappa(u_i)}{4} \right]^2 + \ell_v^{-2}}, \end{aligned} \quad (26)$$

where D_x and D_y are the diagonal elements of the diffusion tensor \mathbf{D} , and ℓ_x, ℓ_y define the characteristic decay lengths along the two principal diffusion axes.

In the continuum limit, the general steady-state solution assumes a path-integral form,

$$\frac{n(u)}{n_0} = \int \mathcal{D}[\mathbf{c}, \mathbf{c}'] \exp \left[\int_0^u d\tilde{u} (\kappa(\tilde{u}) + \mathbf{c}(\tilde{u}) \mathcal{K}_x(\tilde{u}) + \mathbf{c}'(\tilde{u}) \mathcal{K}_y(\tilde{u})) \right], \quad (27)$$

where the functional integral $\int \mathcal{D}[\mathbf{c}, \mathbf{c}']$ represents the sum over all possible sign trajectories for $(\mathbf{c}, \mathbf{c}')$,

$$\int \mathcal{D}[\mathbf{c}, \mathbf{c}'] \cdots = \iint \mathcal{D}[\mathbf{c}] \mathcal{D}[\mathbf{c}'] A[\mathbf{c}, \mathbf{c}'] \cdots \quad (28)$$

We compare the analytical steady-state adatom density field given in Eq. 27, under the mean-field approximation detailed in the Appendix B, for both the biaxial diffusion-dominated condition (i.e., circles with constant curvature) and the curvature-dominated condition (i.e., ellipses with variable curvature). To model the adatom density on the boundary, atoms are initially deposited uniformly within a fixed geometry to mimic the initial epitaxial conditions. The boundary field B acts as a sink potential: once adatoms reach the boundary, they migrate only along it via a projected Langevin dynamics, in contrast to the full 2D Langevin dynamics that govern motion in the bulk.

In Figs. 2, 3, and 4, we systematically investigate QD nucleation profiles in the diluted limit across various boundary geometries, where stochastic seeding events occur exclusively at the boundary. The seeding probability is modulated by the adatom density field, which reflects the combined influences of biaxial diffusion, boundary field effects, and curvature. In the simulations, the ensemble-averaged empirical adatom density field $\langle \hat{n} \rangle$ is obtained from Langevin-based Monte Carlo sampling.

As shown in Fig. 2, this comparison is performed across multiple concentric circular boundaries of varying radii, under both isotropic and anisotropic diffusion conditions (Fig. 2B and 2C). When the QD nucleation potential

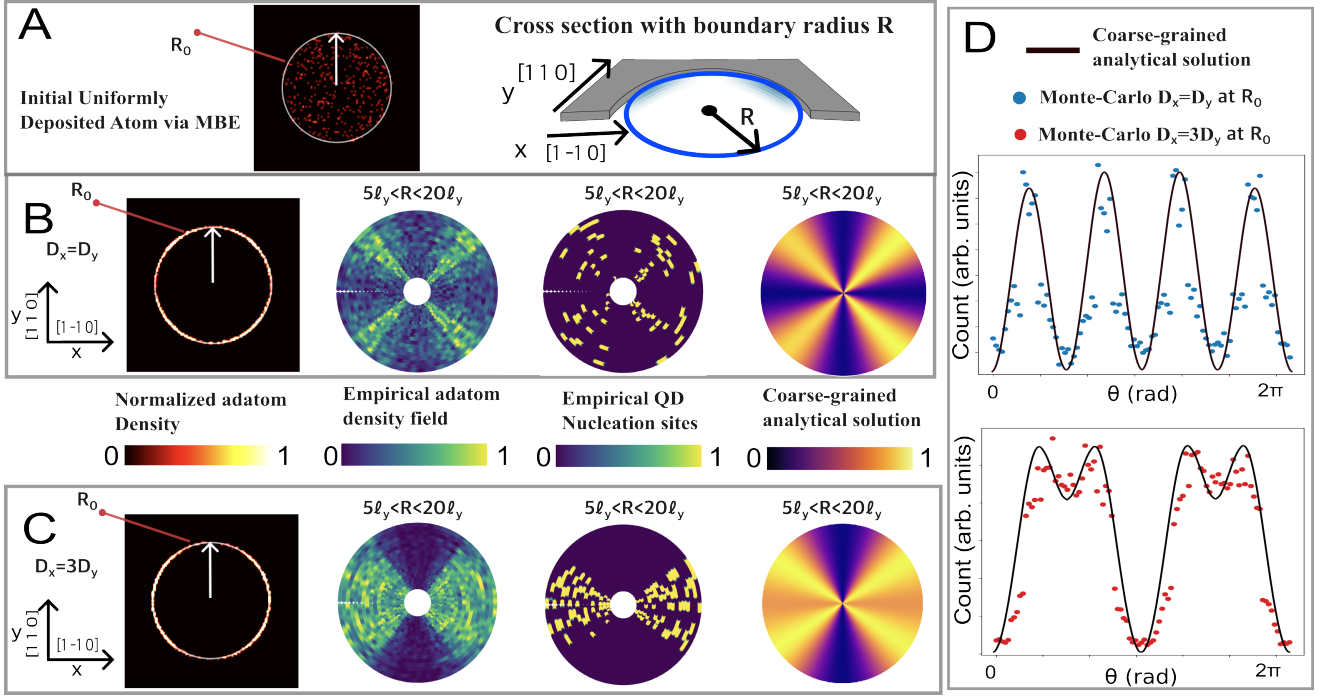


FIG. 2. Detailed comparison of empirical adatom density field (Monte Carlo sampled), QD nucleation, and mean-field analytical adatom density field solutions under a homogeneous circular boundary field, for both isotropic diffusion ($D_x = D_y$) and anisotropic diffusion ($D_x = 3D_y$) along the boundary. **A**: Atomic flux is uniformly deposited from an epitaxy source onto the center of a circular patterned substrate with radius $R_0 = 10\ell_y$, where ℓ_y is the diffusion length in \hat{y} direction. **B–C**: The first (leftmost) column shows the empirical adatom density field at a given radius $R_0 = 10\ell_y$. Due to diffusion, adatoms accumulate at the boundary, and the resulting spatial distribution depends on the diffusion anisotropy. For isotropic diffusion, the empirical density exhibits radial symmetry, while for anisotropic diffusion, the distribution becomes directionally biased. The second column shows radial statistics extracted from various radii with respect to the diffusion length $5\ell_y < R < 20\ell_y$, further illustrating the breakdown of axial symmetry under anisotropy. In both columns, pairwise interactions are turned off ($w = 0$) and the nucleation potential is absent ($V_{nc} = 0$). The third column incorporates a nonzero nucleation potential ($V_{nc} \neq 0$) and displays the resulting QD nucleation sites for various radii $5\ell_y < R < 20\ell_y$. Nucleation events are strongly correlated with regions of high adatom density. The fourth column presents mean-field analytical solutions obtained from Eq. 27. **D**: Cross-section comparison between mean-field analytical solutions and Langevin-based Monte Carlo simulations at a given radius $R_0 = 10\ell_y$, evaluated with respect to angular parametrization under both isotropic and anisotropic conditions.

V_{nc} is included, QDs are distributed along the boundary with spatial profiles that closely resemble the empirical adatom density fields. The spacing between boundary QDs is determined by the interplay of diffusion, geometry, and V_{nc} . For instance, once a QD nucleates at a given location along the boundary, it increases the local chemical potential, generating effective repulsive interactions that redirect subsequent adatoms to other regions.

In Fig. 2D, we construct the analytical solutions of the coarse-grained model under the mean-field approximation and compare them with empirical adatom density results, demonstrating quantitative agreement in capturing the stationary spatial features.

In both isotropic and anisotropic cases, peaks in the adatom density field correspond to regions of enhanced seeding probability, where adatoms are more likely to form temporary clusters. These clusters represent the initial stage of QD formation. Once temporary clusters form in regions of high density, the seeding potential V_{seed}

attracts additional adatoms deposited during heteroepitaxy, leading to the formation of stable QDs along the boundary.

To further quantify the contribution of curvature to the adatom density field along the boundary beyond the case of uniform curvature, we extend the above formulation to elliptical boundary geometries (Appendix C) and shown in Fig. 3A. In Fig. 3B,C, we construct analytical solutions of the coarse-grained model under the mean-field approximation for different axial orientations under both isotropic and anisotropic diffusion, and compare them with the corresponding empirical density fields obtained from Langevin-based Monte Carlo simulations. In regions where the empirical adatom density becomes locally elevated, QD seeding events become statistically favorable. This effect, combined with the fact that regions of high curvature act as effective traps for adatoms, suggests that both biaxial diffusion and local curvature can serve as tuning parameters to control adatom den-

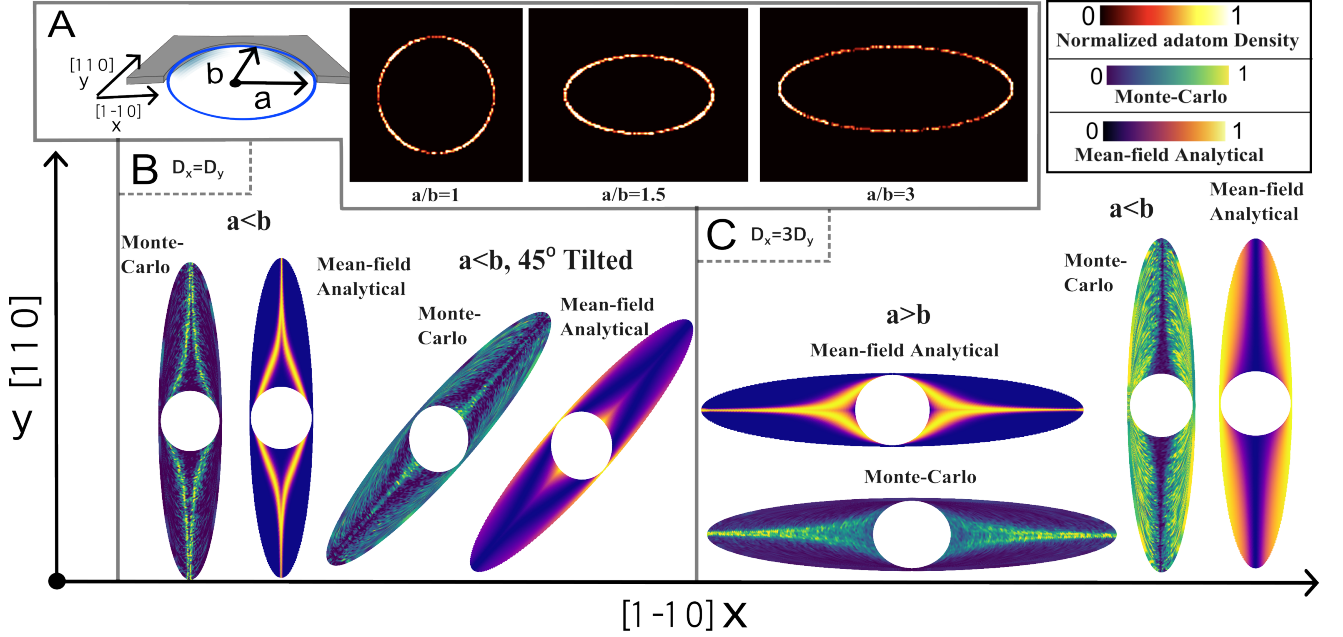


FIG. 3. Detailed comparison between empirical adatom density fields (Monte Carlo) and mean-field analytical adatom density field solutions under a homogeneous elliptical boundary field for isotropic diffusion ($D_x = D_y$) and anisotropic diffusion ($D_x = 3D_y$) along the boundary. **A**: Schematic of elliptical boundaries with varying aspect ratios and the corresponding empirical adatom density fields. **B–C**: Radial statistics extracted from ellipses with different aspect ratios under isotropic diffusion ($D_x = D_y$) and anisotropic diffusion ($D_x = 3D_y$), respectively. The semi-major axis a is oriented parallel ($a > b$), at a 45° tilt ($a < b$), and orthogonal ($a < b$) to one of the diffusion axes \hat{x} . By incorporating local curvature contributions, the resulting mean-field analytical solutions reproduce key features observed in the Monte Carlo-sampled empirical density fields.

sity fields and thus QD nucleation sites along boundary contours. Since boundary geometries can be arbitrarily fabricated, as illustrated in Fig. 4, this approach enables flexible design strategies for device applications.

As the total number of deposited atoms increases, repulsive pairwise interactions w (see Eq. 17) become non-negligible. This results in a modification of the steady-state solution, $n_{\text{int}}(x, y) \sim n(x, y) \exp[q(w)]$, where $q(w)$ is a functional of the interaction strength that broadens the density field along the boundary contour. Intuitively, as repulsive interactions increase, adatoms tend to avoid regions of high density, resulting in a smeared out density profile along the boundary, as shown in Fig. 4A. The governing PDE in Eq. 22 thus becomes coupled through the pairwise interaction term, and nontrivial spatial correlations arising from local curvature and boundary nucleation potentials must be taken into account.

V. SECONDARY QD FORMATION ON PRISTINE SURFACE

A stable InAs/GaAs QD on a pristine surface has a typical size range of 20 to 25 nm, and QD nucleation sites are highly sensitive to material properties and growth conditions. The interaction length scale ℓ_{QD} of the nucleation potential V_{nc} can extend to several tens of nanome-

ters, or even up to hundreds of nanometers, as inferred from the observed relationship between QD density and growth rate [46, 47]. In contrast, stable QDs formed at the boundary often exhibit irregular shapes and stress profiles, which can result in comparable or even greater interaction length scales, ranging from a few nanometers to several hundred nanometers. The repulsive field generated by those stable QDs at the boundary not only affects the migration of nearby adatoms but also interacts with adatom densities in the bulk, influencing the global spatial accumulation and redistribution of newly deposited adatoms, which can be used to statistically control the seeding location on the pristine bulk surface. This concept is illustrated schematically in Fig. 5.

As demonstrated in Fig. 6A, to model boundary-mediated secondary QD nucleation, we begin with a elongated lozenge boundary field design and vary the right-side diagonal coordinate $(a, 0)$ from $-0.6L$ to $2L$, while conserving the total bulk area. The epitaxial deposition of new atoms is introduced sequentially at a rate much slower than the time required for adatoms to reach a steady-state distribution through Langevin dynamics. We then record the spatial distribution corresponding to the first QD nucleation site, as illustrated in the middle panel in Fig. 5. This process is repeated 400 times using different initial random adatom configurations (uni-

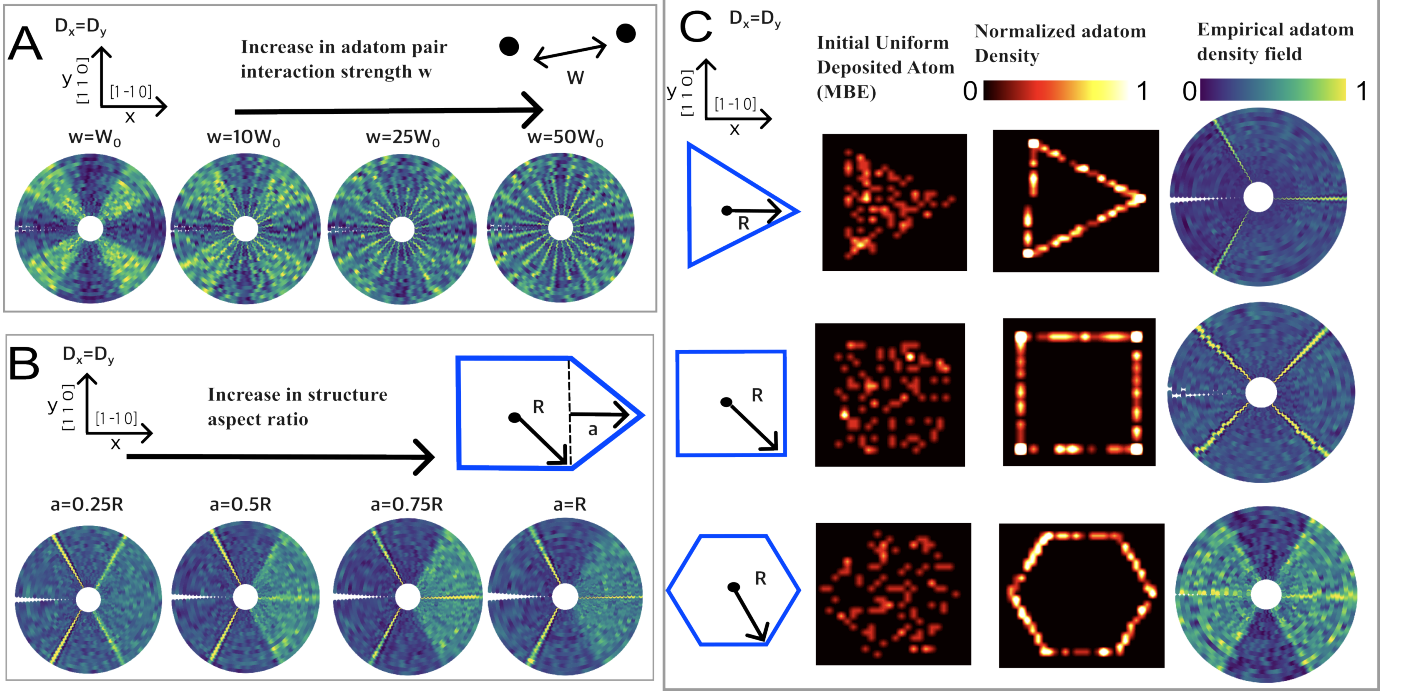


FIG. 4. Geometric tuning of empirical adatom density fields under isotropic diffusion ($D_x = D_y$). **A:** By incorporating a nonzero repulsive pairwise interaction potential w between adatoms, the resulting empirical adatom density field exhibits a smeared-out asymptotic density profile along the boundary contour. **B:** Starting from a lozenge boundary, elongation of the right-side flat edge with an aspect ratio $a = \alpha R$ induces local anisotropic confinement, leading to enhanced adatom accumulation near the elongated region. This demonstrates that local curvature can modulate the spatial profile of the adatom density field along the boundary. **C:** Simulations with various boundary geometries under initially uniform atomic deposition illustrate the flexibility and adaptability of the modeling framework in capturing geometry-tunable adatom density profiles and QD nucleation behavior along the boundary contour.

formly distributed). Depending on the value of a , as shown in Fig. 6B and Fig. 7, the resulting spatial distribution of stable QDs exhibits a boundary-dependent profile. The observed inhomogeneity in the QD distribution reveals statistically preferential nucleation sites. As detailed in Appendix D Fig. 8, we further perform a full parameter sweep over $a \in [-0.6L, 2L]$ for a hexagonal boundary field with a 60° orientation. While the microscopic parameters of the Langevin dynamics remain unchanged, the hexagonal boundary field produces a more spatially extended adatom density field compared to the elongated lozenge boundary field shown in Fig. 7.

VI. DISCUSSION AND CONCLUSION

In this work, we have theoretically and numerically investigated the interplay between geometry, diffusion, and stochastic dynamics in the context of quantum dot (QD) nucleation from empirical adatom density fields. Our results illustrate how geometric properties of boundary contours, such as curvature and orientation relative to anisotropic diffusion axes, along with intrinsic microscopic properties, such as adatom interactions and QD

nucleation dynamics, shape the spatial patterns of QD formation.

In the early stage of epitaxy, referenced as the diluted limit, adatoms are preferentially accumulated along the boundary contour where curvature enhances the local adatom density fields, which can be described by the path integral formulation of a coarse-grained theory. As nucleated QDs accumulate on the boundary, their presence introduces a repulsive interaction field that dynamically alters the chemical potential landscape within the bulk. This feedback mechanism effectively shifts the nucleation zone away from the initial boundary, giving rise to secondary QD populations within the bulk, as demonstrated numerically via the fully scale Langevin dynamics simulations.

While this effect has not yet been experimentally realized, it has broad implications for nanofabrication strategies where precise spatial control of QDs is required in conjunction with complex device architectures. For example, on-chip indistinguishable multi-photon sources require simultaneous electrical tuning and coordination to dynamically bias individual QDs into their trion states, which is essential for constructing large-scale photonic cluster states, a key component of measurement-based

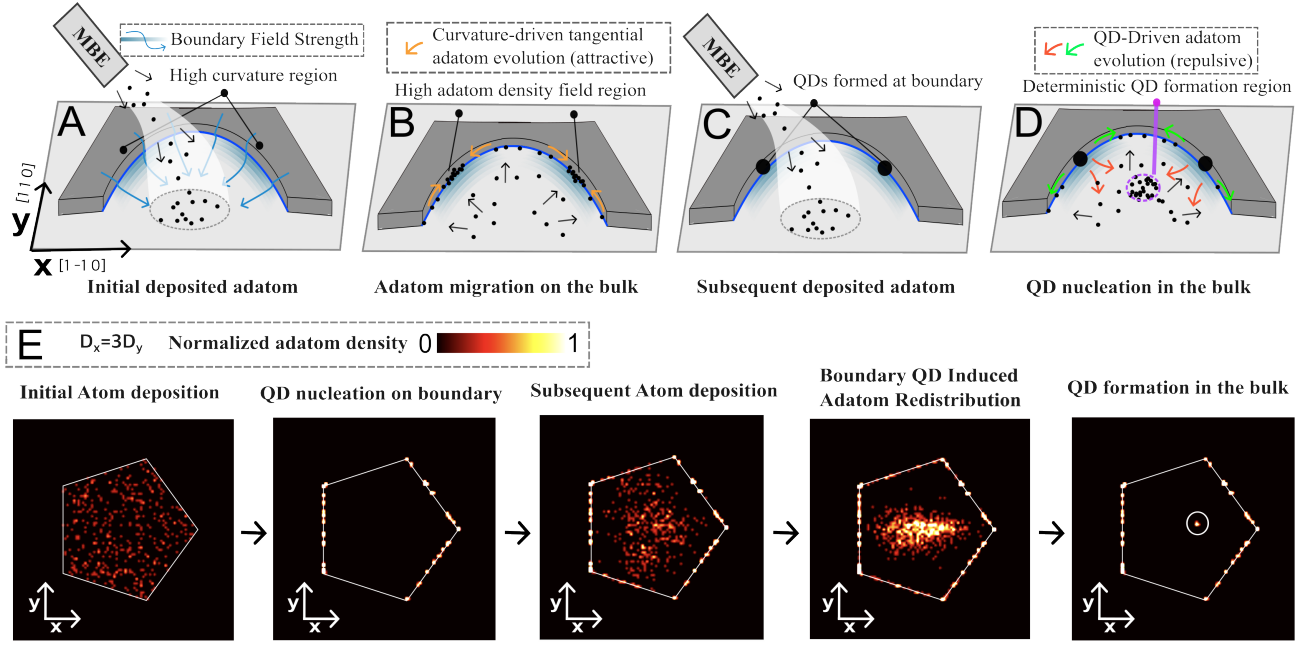


FIG. 5. Schematic of semi-deterministic QD placement guided by a boundary-induced chemical potential landscape. **A**: Atoms are vertically deposited via an epitaxy source onto a patterned substrate with an embedded boundary field (field strength illustrated by the blue gradient), as defined in Fig. 1. **B**: Anisotropic diffusion drives adatoms toward the boundary, where their motion becomes confined upon arrival. As described in Eq. 22, adatoms preferentially cluster in regions of high positive curvature (e.g., concave segments with compressive strain), increasing the local empirical adatom density (black dots) and promoting QD nucleation at these locations. **C**: Following initial QD formation at the boundary, additional atoms are vertically deposited via continued epitaxy at a much lower rate than the rate at which adatoms reach steady state. **D**: The presence of boundary QDs reshapes the local chemical potential landscape. Repulsive interactions from existing QDs redirect adatom migration either tangentially along the boundary (green arrows) or outward into the substrate interior (red arrows). These combined effects promote secondary QD nucleation within the bulk, enabling semi-deterministic and spatially reproducible QD patterning mediated by boundary-induced adatom dynamics. **E**: Snapshots from Monte Carlo simulations where the pentagon boundary profile is used to illustrate each process step described above. Circles indicate stable QDs, while red dots represent adatoms.

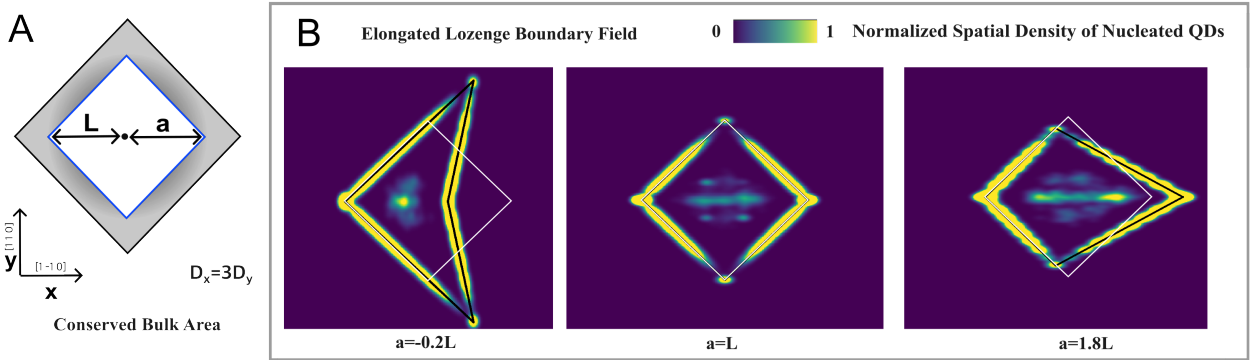


FIG. 6. Boundary-mediated semi-deterministic QD placement via full-scale Langevin dynamics ($D_x = 3D_y$). **A**: A lozenge domain with a tunable right-side diagonal coordinate $(a, 0)$, where $a \in (-0.6L, 2L)$, is used while keeping the total bulk area constant. **B**: Spatial distribution of the first QD nucleation site within the bulk for different aspect ratios, sampled from statistics over 400 distinct random adatom initializations. Although QDs nucleate stochastically, the resulting distribution exhibits statistically localized behavior that is tunable solely through boundary field design, demonstrating the principle of semi-deterministic QD placement. A detailed parameter sweep is provided in the Appendix D, Fig. 7.

quantum computing [48–51]. Furthermore, the controlled spatial arrangement of QDs enables systematic investiga-

tions of decoherence, dissipation, and entanglement propagation in open quantum systems [52, 53], where spatial

correlations and engineered environments play a central role [54, 55].

This work enables the deterministic positioning of high optical quality self-assembled quantum dots on pristine surfaces, opening a new direction for next-generation on-chip photonic devices.

ACKNOWLEDGEMENT

We acknowledge support from NSF Award No. 2427169, 2137740 and Q-AMASE-i, through Grant No. DMR-1906325, and from NWO Quantum Software Consortium (Grant No. 024.003.037). Furthermore, the authors thank Chen Shang and John E. Bowers for their insightful discussions and suggestions.

* zihangwang@ucsb.edu

- [1] T Yoshie, A Scherer, J Hendrickson, G Khitrova, HM Gibbs, G Rupper, C Ell, OB Shchekin, and DG Deppe. Vacuum rabi splitting with a single quantum dot in a photonic crystal nanocavity. *NATURE*, 432(7014):200–203, NOV 11 2004.
- [2] Brian Ellis, Marko Mayer, Gary Shambat, Thomas Sarmiento, James Harris, and Jelena Vučković. Ultralow-threshold electrically pumped quantum-dot photonic-crystal nanocavity laser. *Nature Photonics*, 5:297–300, 2011.
- [3] S. Strauf, K. Hennessy, M. T. Rakher, Y.-S. Choi, A. Badolato, L. C. Andreani, E. L. Hu, P. M. Petroff, and D. Bouwmeester. Self-tuned quantum dot gain in photonic crystal lasers. *Physical Review Letters*, 96(12):127404, 2006.
- [4] JP Reithmaier, G Sek, A Löffler, C Hofmann, S Kuhn, S Reitzenstein, LV Keldysh, VD Kulakovskii, TL Reinecke, and A Forchel. Strong coupling in a single quantum dot-semiconductor microcavity system. *NATURE*, 432(7014):197–200, NOV 11 2004.
- [5] E Peter, P Senellart, D Martrou, A Lemaitre, J Hours, JM Gérard, and J Bloch. Exciton-photon strong-coupling regime for a single quantum dot embedded in a microcavity -: art. no. 067401. *PHYSICAL REVIEW LETTERS*, 95(6), AUG 5 2005.
- [6] S. Strauf, N. Stoltz, M. Rakher, L. A. Coldren, P. M. Petroff, and D. Bouwmeester. High-frequency single-photon source with polarization control. *Nature Photonics*, 1:704–708, 2007.
- [7] H. Snijders, J. A. Frey, J. Norman, V. P. Post, A. C. Gossard, J. E. Bowers, M. P. van Exter, W. Löffler, and D. Bouwmeester. Fiber-coupled cavity-qed source of identical single photons. *Phys. Rev. Appl.*, 9:031002, Mar 2018.
- [8] D. Najer, I. Söllner, P. Sekatski, V. Dolique, M. C. Löbl, M. Renggli, R. Schott, S. Starosielec, S. R. Valentin, R. J. Warburton, A. V. Kuhlmann, A. Ludwig, A. D. Wieck, N. Sangouard, and R. J. Warburton. A gated quantum dot strongly coupled to an optical microcavity. *Nature*, 575:622–627, 2019.
- [9] H. J. Kimble. The quantum internet. *NATURE*, 453(7198):1023–1030, JUN 19 2008.
- [10] Mete Atatüre, Dirk Englund, Nick Vamivakas, Sang-Yun Lee, and Joerg Wrachtrup. Material platforms for spin-based photonic quantum technologies. *NATURE REVIEWS MATERIALS*, 3(5):38–51, MAY 2018.
- [11] C. L. Morrison, R. G. Pousa, F. Graffitti, H. Semenenko, A. S. Rab, B. Fröhlich, A. Montanaro, M. E. Trusheim, D. Englund, J. C. F. Matthews, M. Lobino, and M. G. Thompson. Single-emitter quantum key distribution over 175 km of fibre with optimised finite key rates. *Nature Communications*, 14(1):3573, 2023.
- [12] W. B. Gao, P. Fallahi, E. Togan, J. Miguel-Sanchez, and A. Imamoglu. Observation of entanglement between a quantum dot spin and a single photon. *NATURE*, 491(7424):426–430, NOV 15 2012.
- [13] I. J. Luxmoore, N. A. Wasley, A. J. Ramsay, A. C. T. Thijssen, R. Oulton, M. Hugues, S. Kasture, V. G. Achanta, A. M. Fox, and M. S. Skolnick. Interfacing spins in an ingaas quantum dot to a semiconductor waveguide circuit using emitted photons. *Phys. Rev. Lett.*, 110:037402, Jan 2013.
- [14] J. R. Schaibley, A. P. Burgers, G. A. McCracken, L.-M. Duan, P. R. Berman, D. G. Steel, A. S. Bracker, D. Gammon, and L. J. Sham. Demonstration of quantum entanglement between a single electron spin confined to an inas quantum dot and a photon. *Phys. Rev. Lett.*, 110:167401, Apr 2013.
- [15] Cristian Bonato, Florian Haupt, Sumant S. R. Oemrawsingh, Jan Gudat, Dapeng Ding, Martin P. van Exter, and Dirk Bouwmeester. Cnot and bell-state analysis in the weak-coupling cavity qed regime. *Phys. Rev. Lett.*, 104:160503, Apr 2010.
- [16] M. Kroutvar, Y. Ducommun, D. Heiss, M. Bichler, D. Schuh, G. Abstreiter, and J. J. Finley. Optically programmable electron spin memory using semiconductor quantum dots. *Nature*, 432:81–84, 2004.
- [17] Yu He, Yu-Ming He, Yu-Jia Wei, Xiao Jiang, Kai Chen, Chao-Yang Lu, Jian-Wei Pan, Christian Schneider, Martin Kamp, and Sven Höfling. Quantum state transfer from a single photon to a distant quantum-dot electron spin. *Phys. Rev. Lett.*, 119:060501, Aug 2017.
- [18] Cameron Jennings, Xiangyu Ma, Thushan Wickramasinghe, Matthew Doty, Michael Scheibner, Eric Stinaff, and Morgan Ware. Self-assembled inas/gaas coupled quantum dots for photonic quantum technologies. *Advanced Quantum Technologies*, 3(2):1900085, 2020.
- [19] Tobias Heindel, Je-Hyung Kim, Niels Gregersen, Armando Rastelli, and Stephan Reitzenstein. Quantum dots for photonic quantum information technology. *Adv. Opt. Photon.*, 15(3):613–738, Sep 2023.
- [20] Ming Lai Chan, Alexey Tiranov, Martin Hayhurst Appel, Ying Wang, Leonardo Midolo, Sven Scholz, Andreas D. Wieck, Arne Ludwig, Anders Søndberg Sørensen, and Peter Lodahl. On-chip spin-photon entanglement based on photon-scattering of a quantum dot. *NPJ QUANTUM INFORMATION*, 9(1), MAY 19 2023.
- [21] D. A. Gangloff, G. Éthier Majcher, C. Lang, E. V. Denning, J. H. Bodey, D. M. Jackson, E. Clarke, M. Hugues, C. Le Gall, and M. Atatüre. Quantum interface of an electron and a nuclear ensemble. *Science*, 364(6435):62–66, 2019.

- [22] Pascale Senellart, Glenn Solomon, and Andrew White. High-performance semiconductor quantum-dot single-photon sources. *Nature Nanotechnology*, 12:1026–1039, 2017.
- [23] C Schneider, A Huggenberger, T Sünner, T Heindel, M Strauß, S Göpfert, P Weinmann, S Reitzenstein, L Worschech, M Kamp, S Höfling, and A Forchel. Single site-controlled in(ga)as/gaas quantum dots: growth, properties and device integration. *Nanotechnology*, 20(43):434012, oct 2009.
- [24] Luca Sapienza, Marcelo Davanço, Antonio Badolato, and Kartik Srinivasan. Nanoscale optical positioning of single quantum dots for bright and pure single-photon emission. *Nature Communications*, 6:7833, 2015.
- [25] Imad Limame, Ching-Wen Shih, Alexej Koltchanov, Fabian Heisinger, Felix Nippert, Moritz Plattner, Johannes Schall, Markus R. Wagner, Sven Rodt, Petr Klenovsky, and Stephan Reitzenstein. Epitaxial growth and characterization of multi-layer site-controlled ingaas quantum dots based on the buried stressor method. *Applied Physics Letters*, 124(6):061102, 2024.
- [26] Maxim S. Solodovnik, Danil V. Kirichenko, Denis D. Dukhan, Natalia E. Chernenko, Ivan S. Makhov, Nikita A. Shandyba, Mikhail M. Eremenko, Natalia V. Kryzhanovskaya, and Sergey V. Balakirev. New way to nanopattern gaas surface for subcritical formation of inas quantum dots. *Applied Surface Science*, 688:162373, 2025. Early Access: Jan 2025; Published: Apr 15, 2025.
- [27] Chen Shang, Eamonn T. Hughes, Matthew R. Begley, Rosalyn Kosciwa, Marc Fouchier, Kaiyin Feng, William He, Yating Wan, Gerald Leake, Peter Ludewig, and John E. Bowers. Design rules for addressing material asymmetry induced by templated epitaxy for integrated heteroepitaxial on-chip light sources. *Advanced Functional Materials*, 33(45):2304645, 2023.
- [28] Xiaoyang Zhao, Wen Liu, Yidi Bao, Xiaoling Chen, Chunxue Ji, Guiqiang Yang, Bo Wei, Fuhua Yang, and Xiaodong Wang. Site-controlled growth of in(ga)as/gaas quantum dots on patterned substrate. *Nanotechnology*, 36(5):052001, 2025. Review Article.
- [29] Tatau Nishinaga. 23 - nucleation and surface diffusion in molecular beam epitaxy. In Thomas F. Kuech, editor, *Handbook of Crystal Growth (Second Edition)*, Handbook of Crystal Growth, pages 943–982. North-Holland, Boston, second edition edition, 2015.
- [30] N. Bart, C. Dangel, P. Zajac, et al. Wafer-scale epitaxial modulation of quantum dot density. *Nature Communications*, 13:1633, 2022.
- [31] B.A Joyce, D.D Vvedensky, A.R Avery, J.G Belk, H.T Dobbs, and T.S Jones. Nucleation mechanisms during mbe growth of lattice-matched and strained iii-v compound films. *Applied Surface Science*, 130-132:357–366, 1998.
- [32] V. A. Shchukin and D. Bimberg. Spontaneous ordering of nanostructures on crystal surfaces. *Reviews of Modern Physics*, 71:1125–1171, 1999.
- [33] N. Moll, M. Scheffler, and E. Pehlke. Influence of surface stress on the equilibrium shape of strained quantum dots. *Phys. Rev. B*, 58:4566–4571, Aug 1998.
- [34] Y. Berdnikov, P. Holewa, S. Kadkhodazadeh, et al. Near-critical stranski-krastanov growth of inas/inp quantum dots. *Scientific Reports*, 14:23697, 2024.
- [35] L. Urminen, A. Kuronen, and K. Kaski. Kinetic monte carlo simulation of nucleation on patterned substrates. *Physical Review B*, 66(3):035413, 2002.
- [36] D. Del Gaudio, L. K. Aagesen, S. Huang, T. M. Johnson, B. D. Faeth, H. Lu, R. M. Ziff, and R. S. Goldman. Influence of surface nano-patterning on the placement of inas quantum dots. *Journal of Applied Physics*, 124(11):115307, 2018.
- [37] Arvind Baskaran and Peter Smereka. Mechanisms of stranski-krastanov growth. *Journal of Applied Physics*, 111(4):044321, 2012.
- [38] Kathryn E. Sautter, Kevin D. Vallejo, and Paul J. Simmonds. Strain-driven quantum dot self-assembly by molecular beam epitaxy. *Journal of Applied Physics*, 128(3):031101, 2020.
- [39] J. A. Venables, G. D. T. Spiller, and M. Hanbucken. Nucleation and growth of thin films. *Surface Science Reports*, 12(5):227–365, 1984.
- [40] R. M. Jenkins, G. Baldwin, C. L. Cheung, and S. Krishna. Orientation-dependent pseudomorphic growth of inas for use in quantum dot infrared photodetectors. *Journal of Vacuum Science & Technology B*, 32(2):02C118, 2014.
- [41] Alexander Kley, Paolo Ruggerone, and Matthias Scheffler. Novel diffusion mechanism on the gaas(001) surface: The role of adatom-dimer interaction. *Phys. Rev. Lett.*, 79:5278–5281, Dec 1997.
- [42] M. Yamagiwa, T. Mano, T. Kuroda, T. Tateno, K. Sakoda, G. Kido, N. Koguchi, and F. Minami. Self-assembly of laterally aligned gaas quantum dot pairs. *Applied Physics Letters*, 89(11):113115, 09 2006.
- [43] Herbert B. Callen and Theodore A. Welton. Irreversibility and generalized noise. *Phys. Rev.*, 83:34–40, Jul 1951.
- [44] Hannes Risken. *The Fokker-Planck Equation: Methods of Solution and Applications*. Springer, 2nd edition, 1989.
- [45] Christopher B. Whitehead, Saim Özkar, and Richard G. Finke. Lamer’s 1950 model of particle formation: a review and critical analysis of its classical nucleation and fluctuation theory basis, of competing models and mechanisms for phase-changes and particle formation, and then of its application to silver halide, semiconductor, metal, and metal-oxide nanoparticles. *Mater. Adv.*, 2:186–235, 2021.
- [46] Per Erik Vullum, Magnus Nord, Maryam Vatanparast, Sedsel Fretheim Thomassen, Chris Boothroyd, Randi Holmestad, Bjørn-Ove Finland, and Turid Worren Reenaas. Quantitative strain analysis of inas/gaas quantum dot materials. *Scientific Reports*, 7:45376, 2017.
- [47] T. Konishi, E. Clarke, C. W. Burrows, J. J. Bomphrey, R. Murray, and G. R. Bell. Spatial regularity of inas-gaas quantum dots: Quantifying the dependence of lateral ordering on growth rate. *Scientific Reports*, 7:42606, 2017.
- [48] Xing Ding, Yu He, Z.-C. Duan, Niels Gregersen, M.-C. Chen, S. Unsleber, S. Maier, Christian Schneider, Martin Kamp, Sven Höfling, Chao-Yang Lu, and Jian-Wei Pan. On-demand single photons with high extraction efficiency and near-unity indistinguishability from a resonantly driven quantum dot in a micropillar. *Phys. Rev. Lett.*, 116:020401, Jan 2016.
- [49] Liang Zhai, Matthias C. Löbl, Giang N. Nguyen, Marc Renggli, Johannes Höller, Rüdiger Schott, Andreas D. Wieck, Arne Ludwig, and Richard J. Warburton. Low-noise gaas quantum dots for quantum photonics. *Nature Communications*, 11:4745, 2020. Published 21 September 2020.

- [50] D. Cogan, Z. E. Su, O. Kenneth, E. R. Schmidgall, Y. Don, L. Gantz, I. Schwartz, G. Haim, Y. Benny, O. Raviv, D. Istrati, O. Zilberberg, and D. Gershoni. Deterministic generation of indistinguishable photons in a cluster state. *Nature Photonics*, 17:324–329, 2023. Published 9 February 2023.
- [51] H. Huet, P. R. Ramesh, S. C. Wein, M. Davanco, and K. Srinivasan. Deterministic and reconfigurable graph state generation with a single solid-state quantum emitter. *Nature Communications*, 16:4337, 2025. Published 9 May 2025.
- [52] Zihang Wang and Dirk Bouwmeester. Correspondence between quasiparticle dissipation and quantum information decay in open quantum systems. *Phys. Rev. A*, 110:032407, Sep 2024.
- [53] A.-B.A. Mohamed, H. Eleuch, and C.H. Raymond Ooi. Quantum coherence and entanglement partitions for two driven quantum dots inside a coherent micro cavity. *Physics Letters A*, 383(29):125905, 2019.
- [54] J. Huang, A. Miranda, W. Liu, et al. Spatial quantum-interference landscapes of multi-site-controlled quantum dots coupled to extended photonic cavity modes. *Communications Physics*, 8:152, 2025.
- [55] Daniel Loss and David P. DiVincenzo. Quantum computation with quantum dots. *Phys. Rev. A*, 57:120–126, Jan 1998.

Appendix A: Steady-state Solutions

We first assume $\kappa = 0$, and as an example, the curvature-free steady-state solution in x-direction is given by,

$$T_x^2 D_x \frac{\partial^2 f}{\partial x^2} - \lambda f = 0, \quad f(x) \sim e^{k_x^\pm |x-x_0|}, \quad T_x^2 D_x (k_x^\pm)^2 - \lambda = 0 \implies (k_x^\pm)^2 = \frac{\lambda}{T_x^2 D_x}. \quad (29)$$

In general, the coefficients presented in Eq. 24 have the following form,

$$k_v^\pm = \frac{\kappa T_v D_v \pm \sqrt{(\kappa T_v D_v)^2 + 4 T_v^2 D_v \lambda}}{2 T_v^2 D_v}. \quad (30)$$

Appendix B: Path Integral Formulation and Mean-field Approximation

Starting from a reference point on the boundary, we can obtain a general solution for the coarse-grained adatom density field by considering the following,

$$\begin{aligned} \frac{n(\theta_N)}{n_0} &= \prod_{i=0}^N \sum_{c,c'=\pm 1} A_{c,c'}^i \exp \left(k_x^c |x(\theta_{i+1}) - x(\theta_i)| + k_y^{c'} |y(\theta_{i+1}) - y(\theta_i)| \right) \\ &= \prod_{i=0}^N \sum_{c,c'=\pm 1} A_{c,c'}^i \exp \left(du_i k_x^c |T_x(u_i)| + k_y^{c'} |T_y(u_i)| \right). \end{aligned} \quad (31)$$

We further simplify the above by noting that,

$$k_x^c |T_x(u_i)| = \frac{\kappa}{2} + c \sqrt{\left(\frac{\kappa}{4}\right)^2 + \ell_x^{-2}}, \quad k_y^{c'} |T_y(u_i)| = \frac{\kappa}{2} + c' \sqrt{\left(\frac{\kappa}{4}\right)^2 + \ell_y^{-2}}, \quad (32)$$

where $\ell_x^{-1} = \sqrt{\lambda/D_x}$ and $\ell_y^{-1} = \sqrt{\lambda/D_y}$ represent the diffusion lengths along the x- and y-directions, respectively.

Substituting these expressions, we obtain,

$$\begin{aligned} \frac{n(\theta_N)}{n_0} &= \prod_{i=0}^N \sum_{c_i,c'_i=\pm 1} A_{c_i,c'_i}^i \exp \left[du_i \left(\kappa(u_i) + c_i \sqrt{\left(\frac{\kappa(u_i)}{4}\right)^2 + \ell_x^{-2}} + c'_i \sqrt{\left(\frac{\kappa(u_i)}{4}\right)^2 + \ell_y^{-2}} \right) \right] \\ &= \sum_{\mathbf{c},\mathbf{c}'} A_{\mathbf{c},\mathbf{c}'} \prod_{i=0}^N \exp \left[du_i \left(\kappa(u_i) + \mathbf{c}_i \sqrt{\left(\frac{\kappa(u_i)}{4}\right)^2 + \ell_x^{-2}} + \mathbf{c}'_i \sqrt{\left(\frac{\kappa(u_i)}{4}\right)^2 + \ell_y^{-2}} \right) \right], \end{aligned} \quad (33)$$

where, $\mathbf{c} = [1, -1, 1, 1, \dots]$, $\mathbf{c}' = [-1, -1, 1, -1, \dots]$, are sequences (or path) of signs c_i indexed by $i = 0, \dots, N$. The summation is taken over all possible combinations of \mathbf{c} and \mathbf{c}' , representing distinct sign trajectories (path) within the exponential.

In the continuum limit, the product becomes an integral in the exponent, leading to the following path integral representation,

$$\frac{n(u)}{n_0} = \int \mathcal{D}[\mathbf{c}] \mathcal{D}[\mathbf{c}'] A[\mathbf{c}, \mathbf{c}'] \exp \left[\int_0^u d\tilde{u} (\kappa(\tilde{u}) + \mathbf{c}(\tilde{u}) \mathcal{K}_x(\tilde{u}) + \mathbf{c}'(\tilde{u}) \mathcal{K}_y(\tilde{u})) \right], \quad (34)$$

as discussed in Eq. 27.

The above path integral formulation can be numerically approximated under a mean-field assumption by directly evaluating the defining expression,

$$\begin{aligned} n(\phi, \theta_0) &\sim \sum_{\mathbf{c}, \mathbf{c}'} \exp \left[\sum_{i=0}^{\phi} \kappa(u_i) (x(\theta_{i+1}) - x(\theta_i) + y(\theta_{i+1}) - y(\theta_i)) \right] \\ &\approx \exp [\kappa(\phi) (R(D_x)(x(\phi) - x(\theta_0)) + R'(D_y)(y(\phi) - y(\theta_0)))] \\ &\quad + \exp [-\kappa(\phi) (R(D_x)(x(\phi) - x(\theta_0)) + R'(D_y)(y(\phi) - y(\theta_0)))] , \end{aligned} \quad (35)$$

where $R(D_x)$ and $R'(D_y)$ are signed (parametrization-dependent) coefficients. In the last line, only two overall sign contributions are retained, consistent with the endpoint (mean-field) treatment of the path sum.

To obtain the ensemble-averaged density, we further sum over all possible starting points θ_j ,

$$n(\phi) \sim \sum_{j=0}^{2\pi} n(\phi, \theta_j). \quad (36)$$

The above mean-field solutions are numerically demonstrated on circular and elliptical boundary fields presented in Fig. 2 and Fig. 3.

Appendix C: Elliptical boundary parametrization

Consider an isotropic diffusion setting with $D_x = D_y$, and an elliptical boundary confinement centered at the origin, characterized by a semi-major axis a and a semi-minor axis b (as shown in Fig. 3A). The boundary is parametrized by $\theta_0 \in [0, 2\pi)$, corresponding to a boundary point located at $[a \cos \theta_0, b \sin \theta_0]$.

For simplicity, we define the local configuration space using a second ellipse with the same aspect ratio, scaled by a global constant r , such that,

$$\mathbf{r}_{\text{bd}}(r, \phi, \theta_0) = a(r \cos \phi - \cos \theta_0) \hat{\mathbf{x}} + b(r \sin \phi - \sin \theta_0) \hat{\mathbf{y}}. \quad (37)$$

The local curvature at the boundary point (i.e., when $r = 1$) takes the form,

$$\kappa(\theta_0) = \frac{ab}{(b^2 \cos^2 \theta_0 + a^2 \sin^2 \theta_0)^{3/2}}. \quad (38)$$

Analytical solutions of the adatom density field under the mean-field approximation (Eq. 35) show close agreement with the results obtained from direct simulations of adatom Langevin dynamics sampled via Langevin-based Monte-Carlo (Fig. 3B,C).

Appendix D: Boundary-mediated semi-deterministic QD placements under different geometries

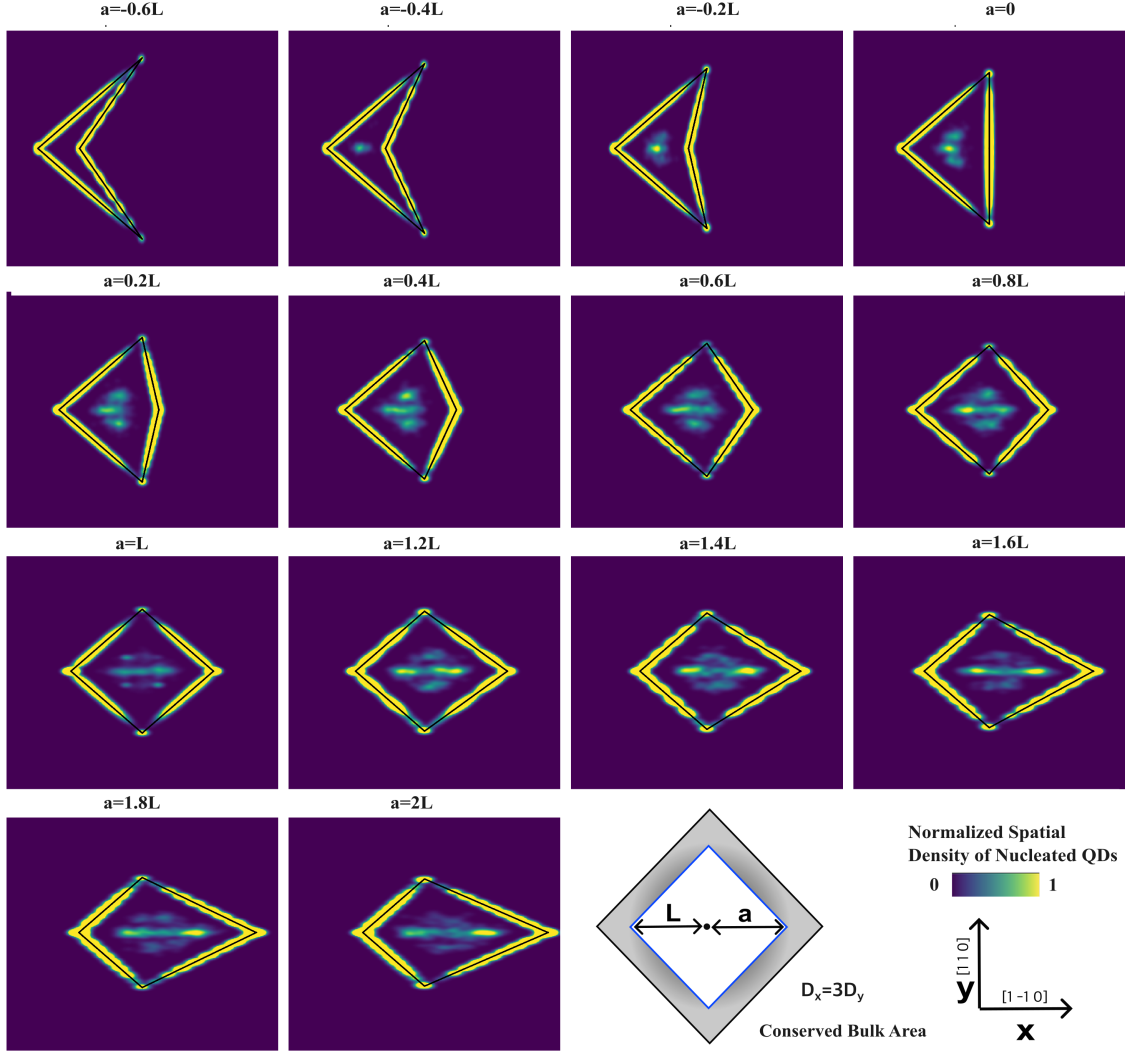


FIG. 7. Full parameter sweep over $a \in [-0.6L, 2L]$ for the elongated lozenge boundary field presented in Fig. 6

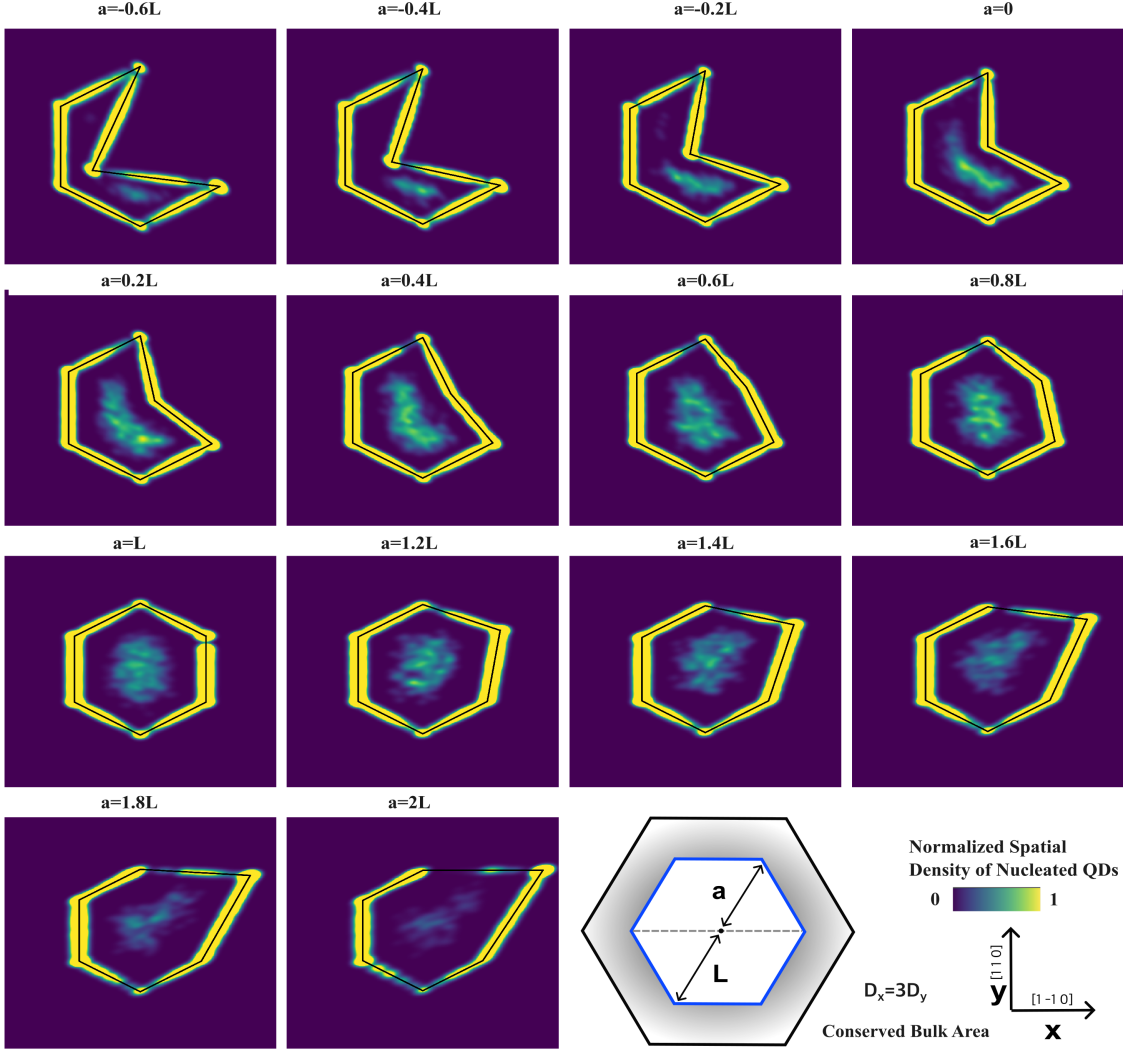


FIG. 8. A full parameter sweep over $a \in [-0.6L, 2L]$ for the hexagonal boundary field at 60° angle.